Research Square

Preprints are preliminary reports that have not undergone peer review.
They should not be considered conclusive, used to inform clinical practice,
or referenced by the media as validated information.

The Uruana de Minas magnetic anomaly within the South Atlantic Anomaly: regional-field control and limits of cross-survey prediction

Lucas Giovani Ribeiro

coin26@mail.com

Independent Researcher

Marcos André Simonssini

Independent Researcher

Research Article

Keywords:

Posted Date: November 17th, 2026

DOI: https://doi.org/10.21203/rs.3.rs-11641080/v1

License: This work is licensed under a Creative Commons Attribution 4.0 International License.
Read Full License

Additional Declarations: No competing interests reported.

The Uruana de Minas magnetic anomaly within the South Atlantic Anomaly: regional-field control and limits of cross-survey prediction

Lucas Giovani Ribeiro and Marcos André Simonssini

Independent researchers, Uruana de Minas, Minas Gerais, Brazil
Corresponding author: Lucas Giovani Ribeiro · coin26@mail.com
ORCID: Lucas Giovani Ribeiro 0009-0002-1417-0062; Marcos André Simonssini 0009-0000-9076-6410

Abstract

Updating the geomagnetic field epoch improves historical profile prediction at Uruana de Minas, Brazil, within the South Atlantic Anomaly. We quantify this improvement and the stability of local-gradient reconstruction. On five adjacent eastern lines of the 2011 survey, subtracting the core field modeled by the Enhanced Magnetic Model 2017 (EMM2017) reverses the northern slope; subtracting its resolved lithospheric contribution preserves all five positive slopes. This separation holds across five processing stages and two estimators. Among 23 Brazilian sectors compared under common modeled backgrounds, only Uruana reproduces both the 2008 and 2011 sign sequences. Updating the field epoch in a model fitted to 2008 reduces 1971–1972 profile-shape error by 32.1% on 75 nearby segments; the reduction remains positive across nine depth–damping settings (10.6–35.2%). However, 18 source-model configurations predict positive target slopes on all 14 lines observed as negative in 2011. Off-grid synthetic tests expose depth-dependent sign recovery even without noise. Within the primary equivalent-source family, imposing negative slopes on all 14 lines increases the regularized objective by 8.4% and the 2008 root-mean-square fitting error from 1.007 to 1.116 nT. Together, the field decomposition, historical evaluation and resolution audit distinguish background-controlled sign changes from unstable cross-survey predictions, providing separate tests of epoch correction and local-gradient recovery.

Keywords South Atlantic Anomaly, aeromagnetics, secular variation, magnetic gradient, equivalent sources, resolution

1. Introduction

In the 2011 aeromagnetic survey at Uruana de Minas, Brazil, intensity falls with grid north on every line between 6 and 8 km north of the survey center. The modeled main field rises across this same target window. Farther north, between 16 and 20 km, measured intensity rises again. Ribeiro and Simonssini (2026) described the raw-field reversal in a preprint. Uruana lies within the South Atlantic Anomaly (SAA), a broad minimum in Earth's main-field intensity. Finlay et al. (2020) traced its evolution to changes in the core field. Poletti (2021) reconstructed historical field changes in the Jequitinhonha and Mucuri valleys of eastern Brazil.

Brazilian aeromagnetic compilations combine surveys flown decades apart and at different elevations. Spatial differences in secular variation affect reduction to a common epoch (Vujić and Brkić 2016), while downward continuation and source regularization can limit the recovery of shorter-wavelength structure (Zuo et al. 2020). Evaluations of airborne-field inversion distinguish agreement with external observations from internal uncertainty estimates (Foroughi et al. 2025). A

reduction in historical profile error and the recovery of a local gradient sign therefore require separate tests.

We connect three diagnostics: separation of modeled core and resolved lithospheric contributions along the 2011 profiles; comparison of the joint 2008 and 2011 sign pattern across 23 sectors under common backgrounds; and historical prediction followed by an explicit audit of local-gradient recovery. The 2008 source fit improves historical profiles when the field epoch is updated, yet predicts the wrong target sign on every 2011 line. Known-source experiments and constrained ridge solutions test how sensitive that prediction is to source resolution and the fit–regularization tradeoff. The contribution is a quantitative separation of background dependence, epoch-correction benefit and conditional sign stability for the same survey system.

2. Two scales and three surveys

Secular variation changes both the direction onto which a crustal magnetic field projects and the direction and strength of induced magnetization. Lesur and Gubbins (2000) used this dependence to investigate crustal sources. The Uruana survey center lies at 16.0593° S, 46.2585° W. Using the 28 μT surface contour as a geographic convention (Pavón-Carrasco and De Santis 2016), the center falls inside the SAA at the three survey epochs. The International Geomagnetic Reference Field, generation 14 (IGRF-14), gives 24.580 μT there for 1971.5, 23.659 μT for 2008.5 and 23.623 μT for 2011.5 (Beggan et al. 2026). Fig. 1 shows the contour and the historical evaluation tracks.

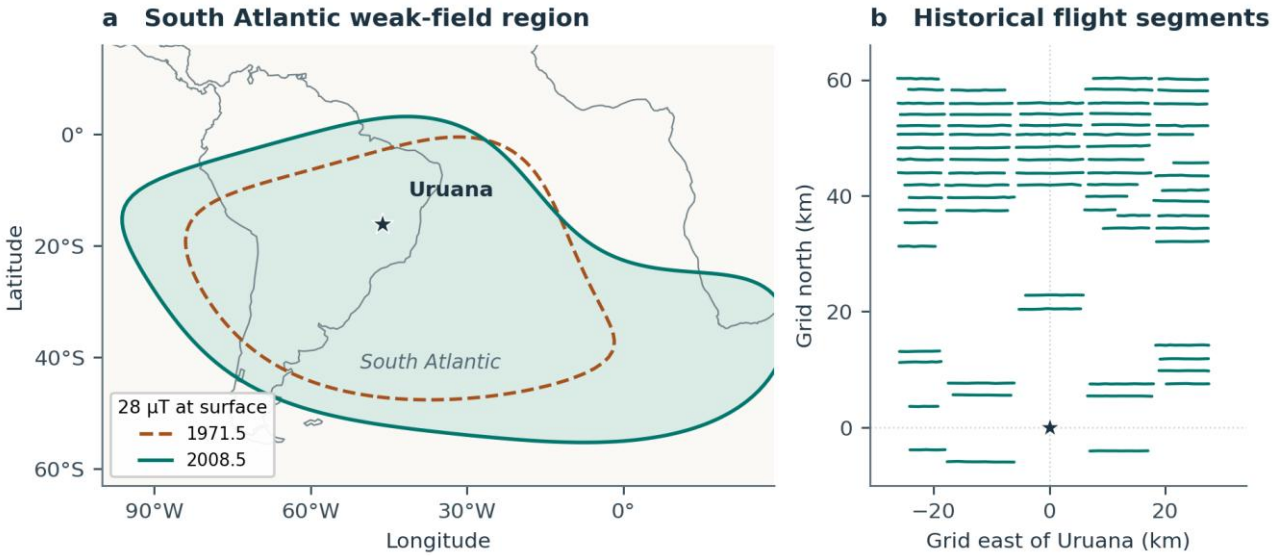


Fig. 1 Geographic relationship between the two scales. (a) The star marks Uruana against surface IGRF-14 contours. Shading shows the area below 28 μT in 2008.5. Coastlines are from Natural Earth at 1:110 million. (b) Each trace follows one of the 75 historical evaluation segments. The star is the same center, in UTM zone 23S coordinates relative to Uruana. The sample extends mainly north of the site. Code in Online Resource 1 (figures/fig.py)

2.1 Survey records

The 2008 ANP São Francisco Norte survey (project 0032) supplies the grid for the cross-survey comparison and the source models. The 1.5 km grid contains two total-field channels, Mag and its diurnally corrected counterpart, mag_var. We tested the sign sequence in both channels and fitted the sources for historical profile reconstruction to mag_var. The orbital sensitivity test (Section 8.2) uses both channels. Nominal measurement-line spacing was 6 km. The aircraft flew at 2.1–2.3 km elevation. We used a 2.2 km flight plane.

For 1971–1972 we used the digitized PGW profiles from SGB/CPRM project 1009 (Convênio Geofísico Brasil–Alemanha). PGW reports magnetic residuals after IGRF reduction. The alternative WMC product carries an undocumented additive offset (Monteiro 2002). The distributed PGW subset identifies production lines and barometric levels (0.79 or 0.95 km nearby) but gives no line-specific flight dates. We used 1971.5 as a single representative epoch and tested dates spanning both acquisition years (Section 6.2). The 2011 Formoso–Buritis–Lagoa Grande survey (SGB/CPRM project 3087) provides original total-field readings (MAGBRU) and GPS altitudes.

3. The main field restores the northern rise on the eastern lines

All 14 flight lines cross two windows north of the survey center. Magnetic intensity decreases with grid north in the target window (6–8 km) and increases in the northern window (16–20 km). We evaluated IGRF-14 at the position and GPS height of each 250 m bin and subtracted its total intensity from the measured intensity. Subtracting IGRF-14 preserves the negative target slope on all 14 lines. In the raw least-squares fits, eight lines retain a positive northern slope after subtraction. On the other six, the northern slope is positive in the measurements and negative in the residuals (Fig. 2a).

Five of these six lines are adjacent on the eastern side of the sampled tracks (12430–12470). Their northern residual slopes are negative and their measured slopes positive for all five archived total-field products under both ordinary least squares and Theil–Sen estimation. We fitted each estimator directly to the total and residual profiles. The sixth line, 12380, changes sign only for least-squares fits to the raw and compensated products. On the five eastern lines, the sign change survives every eligible single-bin omission under all ten configurations (85 distinct omissions). Across those omissions, the largest residual slope was −0.171 nT/km and the smallest measured slope was +0.179 nT/km. Online Resource 1 gives the results for all 14 lines.

Only Uruana matched both surveys at a common modeled location in the comparison with 22 neighboring sectors. We held each sector's measured residuals and survey geometry fixed and substituted the main field for each survey year. For all signs to hold, the smallest slope measured in its required direction must be positive. Across the 64,800 locations, Uruana reached +0.429 nT/km on this criterion. The highest-scoring control, 14 km west, reached −0.203 nT/km (Fig. 2b). Section 4 gives the survey criteria and the tests of processing sensitivity.

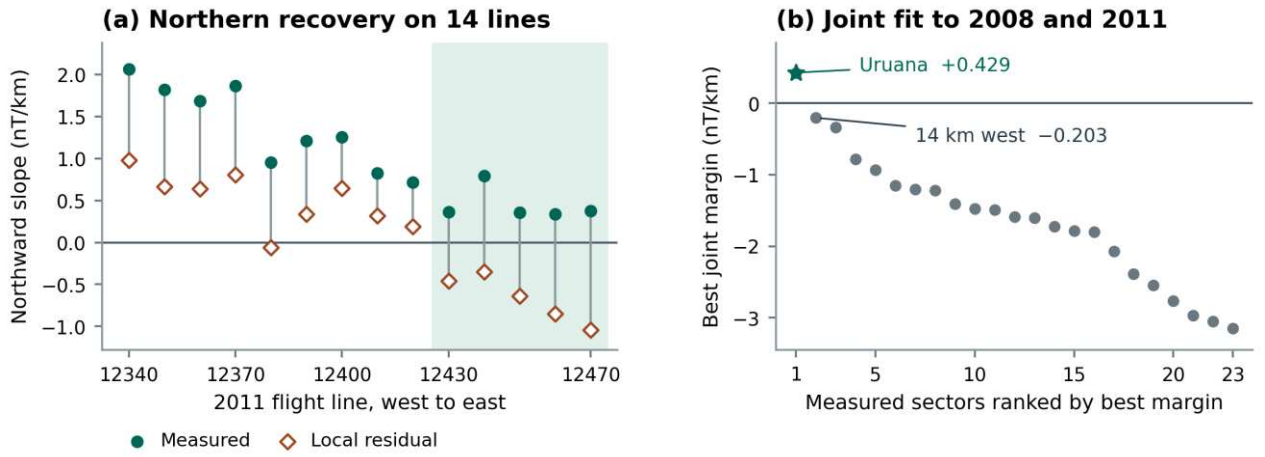


Fig. 2 (a) Raw-field least-squares slopes in the northern window. Each segment joins the measured slope to the slope after IGRF-14 subtraction. Shading marks the five lines on which subtraction reverses the sign under all ten configurations. (b) Each point is a measured sector. Its best joint margin is the maximum, across the 1° grid, of the smallest signed slope required in both surveys. Positive values satisfy every sign constraint. Code in Online Resource 1 (local_recovery/figure.py)

3.1 The regional gradient along the flight lines

We evaluated the northward slope of total intensity at the 2011 bin positions and GPS elevations, first using the tilted, centered IGRF-14 dipole, then using the complete field. The tilted dipole and complete field give opposite gradient signs in both windows on all 14 lines (Fig. 3). In the 6–8 km target, the median slopes are −1.802 nT/km for the dipole and +1.011 nT/km for the full field. The survey provider's archived IGRF column gives +1.009 nT/km. Measured slopes have a median of −1.540 nT/km. In the 16–20 km northern window, medians for the dipole, full field and observations are −1.767, +1.029 and +0.888 nT/km, respectively. Both modeled signs persist at constant altitude on all lines.

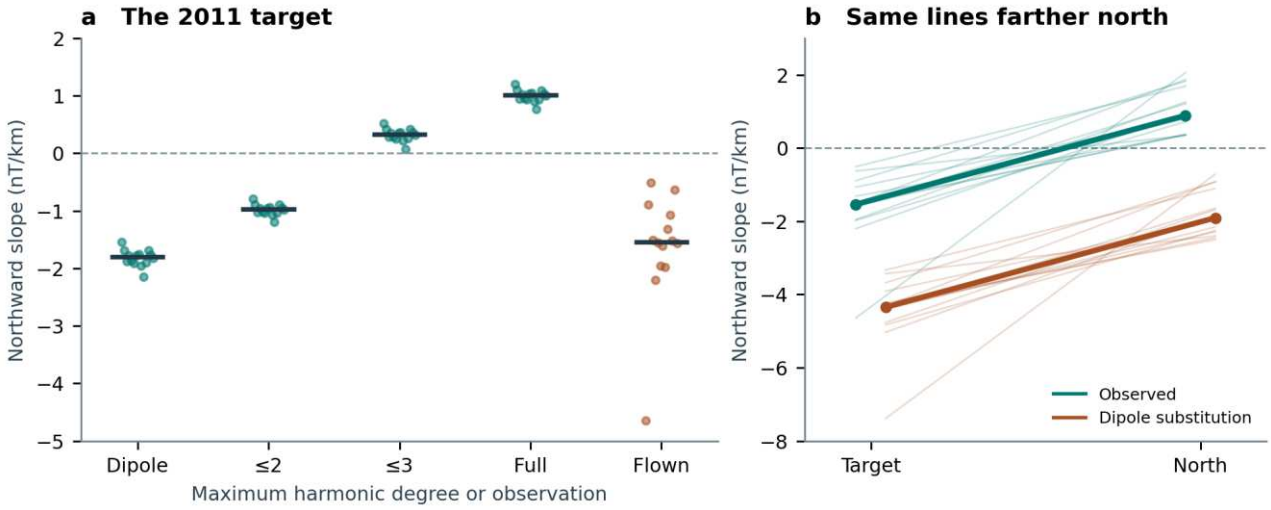


Fig. 3 (a) Each dot is one flight line. Short bars give medians. Successive field models include degrees 1, 1–2, 1–3 and 1–13. (b) Thin segments link the two windows on the same line, and heavy segments join medians. Dipole substitution adds the dipole intensity to the observed scalar residual relative to the full main field, at each bin. Code in Online Resource 1 (nested_gradients/plots.py)

On the five eastern lines, the northern slope changes sign when we remove the low-degree field modeled by EMM2017. We evaluated EMM2017 (NOAA NCEI 2017) at each bin's position and GPS height for 2011.5. To isolate the modeled lithospheric contribution to total intensity, we subtracted

the core-field intensity (degrees 1–15) from the full-field intensity (degrees 1–790). Removing that increment from the observations left all five northern slopes positive in all ten configurations (+0.109 to +0.695 nT/km). Removing the core field alone reversed all five (−1.040 to −0.211 nT/km), as did removing the full field (−1.083 to −0.339 nT/km). The five reversals also persisted when we added EMM2017 degrees 134–400 to the IGRF-14 vector before computing and subtracting its intensity (−1.007 to −0.129 nT/km). That band spans wavelengths of about 100–300 km. The full model resolves wavelengths down to about 51 km. Evaluating the modeled backgrounds at a common 1.0 km ellipsoidal height while retaining the flown measurements gives the same separation. Across all five lines and ten fits, lithospheric subtraction leaves +0.119 to +0.693 nT/km and core-field subtraction leaves −0.904 to −0.320 nT/km (Online Resource 1, spatial_sensitivity/height_sensitivity.csv).

$$\Delta F_{lith} = \|B_{1-790}\| - \|B_{1-15}\| \quad (1)$$

Here B denotes a modeled vector field and the subscripts give its retained spherical harmonic degrees. Equation (1) is the lithospheric increment in total intensity, rather than the magnitude of the lithospheric vector alone. For ordinary least squares on identical bins, subtracting a background subtracts its fitted slope exactly. Theil–Sen slopes are recomputed from the subtracted profiles because that estimator is not additive. The comparison attributes the five northern sign changes to the modeled core-field background at the resolved wavelengths; it does not identify the source of the shorter-wavelength local residual.

3.2 Contributions of the quadrupole and octupole

Hartmann and Pacca (2009) related the quadrupole and octupole to the large-scale South Atlantic weak field. Along the 2011 tracks, the main-field gradient in the target window is negative on all 14 lines through degree two and positive on all 14 through degree three. As a post hoc check we subtracted each single spherical harmonic degree from the complete vector field before computing intensity. Omitting either degree two or three restored negative slopes on all 14 lines. Omitting any one degree from four through thirteen preserved positive slopes on all 14. Adding either degree alone to the dipole left the slope negative.

Holding the measured scalar residual fixed and substituting dipole intensity made both windows negative on all 14 lines. The northern slope still exceeded its paired target slope on every line (median contrast +2.414 nT/km, compared with +2.564 nT/km as flown). This substitution changes the regional background while preserving the measured local contrast.

4. Testing the Uruana pattern in 22 neighboring sectors

We translated the 2011 window pair to a grid of 51 sector origins. East offsets ranged from −56 to +56 km in 7 km steps, the width of 14 nominal 0.5 km line spacings, with north offsets of −32, 0 and +32 km. Each sector used a distinct group of 14 nominal line identifiers for its east position, with the same identifiers revisited at different north offsets. We cropped the raw samples to the same target and northern windows before binning. Per line we required at least 4 and 8 bins spanning at least 0.75 and 2 km in the target and return, respectively. Of 24 sectors with 14 paired lines, three satisfied the dipole-negative and full-field-positive reference conditions in both windows and the observed negative-to-positive sequence on all lines. These were Uruana and sectors 35 and 49 km east, both 32 km north. The compensated channel selected the same three.

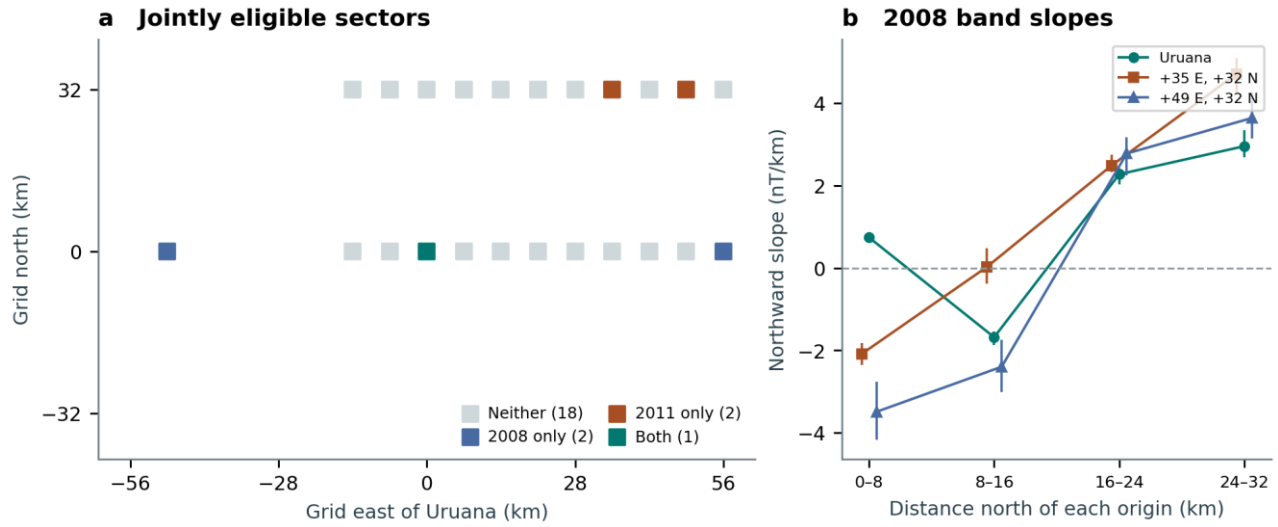


Fig. 4 (a) Outcomes for the 23 sectors eligible in both surveys. Unsampled or ineligible origins have no symbol. (b) The three 2011-positive sectors in the 2008 survey. Each point is the median across the two channels and five corridor widths. Vertical ranges span the ten estimates. All four signs must hold in every realization. Code in Online Resource 1 (nested_gradients/plots.py)

At all origins we applied the four-band 2008 rule used in the earlier Uruana analysis (Ribeiro and Simonssini 2026). The slopes in successive 8 km bands must be positive, negative, positive and positive in both channels at corridor half-widths of 0.75, 1.5, 3, 6 and 9 km. Each band requires at least four native rows and 80% grid support. Of the 24 sectors with complete 2011 pairs, the sector 49 km west and 32 km south lacked the required 2008 grid support. Among the 23 jointly eligible sectors, the two criteria selected three sectors each and intersected only at Uruana. The two northeastern sectors each failed the 2008 rule in all ten realizations. Keeping 2008 scalar residuals fixed and substituting the dipole removed the Uruana pattern in all ten. The earlier study reported Uruana as the sole joint pass in 82 centers under a different 2011 screen. Fig. 4 shows the 23 sectors eligible under the present criteria.

At Uruana a uniform added northward slope preserves all observed signs in both surveys only in the open interval −0.339 to +0.507 nT/km (rounded endpoints). The constraints come from the least positive northern and least negative target slopes in 2011. In a 1° longitude sweep at Uruana's latitude in 2011.5, the dipole-to-full sign change occurred at 82 of 86 longitudes inside the 28 μT contour and 60 of 274 outside. The dipole-to-full sign change therefore extends across the 28 μT contour along this parallel.

4.1 Substituting the regional background at fixed survey geometry

We subtracted the local IGRF-14 intensity at each measured point, carried its scalar residual, height and horizontal offsets to a new center, and added the modeled intensity there at the original epoch. The WGS84 tangent planes preserve orientation relative to true north. We scored all 14 target/north line pairs in 2011 and the four 2008 bands in both channels at five corridor widths. The transported scalar residual retains the combined effects of source magnetization and field projection at the original site.

This is a counterfactual test of background-gradient compatibility. It does not physically relocate a magnetized body or predict how its induced magnetization would change at the destination. The

historical equivalent-source test in Section 5 separately changes the projection and induced-moment directions.

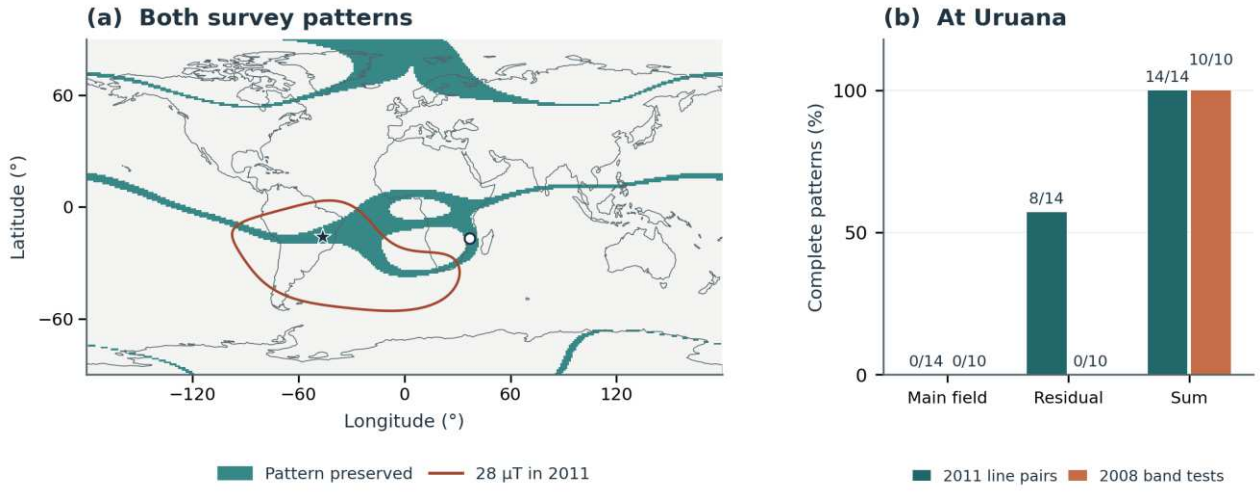


Fig. 5 Shading marks 1° grid centers where both transported surveys pass. The star marks Uruana and the circle marks the Mocuba comparison. The bars show counts of complete two-window line pairs and four-band tests at Uruana. Code in Online Resource 1 (background_transplant/figure.py)

At Uruana, the main field alone reproduced 0 of 14 line pairs and the residual alone reproduced 8 of 14. In 2008 the residual alone failed the first band at every width in both channels. Their sum reproduces 14 of 14 pairs and all 10 four-band tests by construction. Holding residual slopes fixed and multiplying each main-field slope by the same factor preserves every sign only between 0.737 and 1.535 (open bounds, rounded). Both limits come from 2011.

Across 64,800 grid centers, the main field alone reproduced the two-survey pattern nowhere. With the residuals restored, it survived over 23.1% of the area below 28 μT at both dates and 6.8% of the area outside at both dates. Every passing 2011 location also passed in 2008. Along Uruana's latitude, 290 of 339 interior longitudes passed, versus 32 of 1,094 exterior longitudes at 0.25° spacing. Seven changed class between epochs. Of the 32 exterior matches, 31 formed a single interval from 33.875°E to 41.375°E. At Mocuba, Mozambique, the modeled field preserved all the Brazilian signs in the raw least-squares test at a surface intensity of 31.6 μT in both years. Fig. 5 maps the modeled matches and shows the contributions at Uruana.

4.2 Only Uruana matches both surveys at the same modeled locations

We repeated the geographic substitution for all 23 eligible sectors. Each sector retained its own 2011 flight tracks, heights and scalar residuals, and its own 2008 grid values and geometry. The same destination center supplied the main fields for both dates. A match required negative target and positive northern slopes on all 14 lines in 2011 and the four-band sequence in both 2008 channels at all five widths. We scored the 68 measured-sign constraints independently of the dipole sign. The smallest signed slope defines the joint margin. It is positive when every required sign holds.

On the 1° grid, eight sectors met the 2011 criterion at one or more destinations and nine met the 2008 criterion. Three appeared in both lists. For the sectors 7 and 14 km west of Uruana, the sets of passing locations for the two epochs were disjoint (Table 1). Uruana alone had a common set,

comprising 5,522 grid centers. The 2° grid selected the same sector. Substitution using the compensated 2011 channel also selected only Uruana (5,915 centers on the 1° grid).

Table 1 Counts and percentages of the 64,800 destination centers on the 1° grid. These three Brazilian sectors met each year's criterion at one or more destinations. The two single-year columns include any joint matches. The last column requires both years to pass at the same destination

Measured sector	2008	2011	Both years
Uruana	14,898 (22.99%)	5,522 (8.52%)	5,522 (8.52%)
7 km west	2,626 (4.05%)	352 (0.54%)	0 (0%)
14 km west	986 (1.52%)	9,594 (14.81%)	0 (0%)

The best joint margin on the 1° grid was +0.429 nT/km for the Uruana residuals and −0.203 nT/km for the closest competitor, 14 km west. Refining around each sector's best grid center gave +0.431 and −0.196 nT/km, respectively. In a post hoc sensitivity test on the 1° grid, we allowed each sector to discard its most adverse 2011 line and its most adverse 2008 corridor width at each location. All 22 controls still failed. The best relaxed margin among them was −0.065 nT/km, again for the sector 14 km west.

4.3 Sensitivity to processing and slope estimation

The project 3087 archive contains uncompensated, compensated, diurnally corrected, leveled and microleveled versions of the 2011 total field (Microsurvey 2011). We reduced the same 239,118 flight records to 8,009 occupied 250 m bins in the 23 sectors. For each product we repeated the geographic test with ordinary least squares and with the median of all pairwise slopes (Theil–Sen) in both years. We recomputed each estimate after substituting the field at each destination. We retained both 2008 channels and the original corridor widths and elevation rules.

At Uruana all 14 line pairs passed in each of the ten fits to the same flight measurements. Across the global grid, each of the ten configurations selected Uruana and no other sector, including when the most adverse line and corridor width were both omitted. Requiring the complete pattern at the same location in all ten configurations reduced the common set to 731 grid centers. At Uruana's latitude, 73 of 339 longitudes below 28 μT in both years (21.5%) and six of 1,094 longitudes above that threshold in both years (0.55%) passed this stricter rule. The corresponding global within-class area fractions were 4.68% and 1.30%.

Line 12350 had the raw Theil–Sen target slope closest to zero (−0.00143 nT/km, Supplementary Fig. S2). After removing one occupied 250 m bin at a time from the native Uruana data, 346 of 348 omissions preserved all 14 pairs with raw least squares and 346 with raw Theil–Sen. One bin on line 12350 affected both estimators. On the microleveled channel, 347 of 348 omissions retained all pairs with each estimator. Every omission preserved the northern recovery on all 14 lines. At the 14 km western control, applying the diurnal correction changed the 28 native least-squares slopes by a median absolute 0.073 nT/km. The median change exceeded the 0.065 nT/km shortfall under the relaxed raw-field rule, yet the corrected control profiles still failed.

We tested sensitivity to spatially correlated changes by perturbing the fitted profile residuals in contiguous northing strips and repeating the raw least-squares search on the full 1° grid. Each draw used the same random sign for all lines, bands, channels and widths sharing a strip within a survey. Strip widths were 0.5 km in 2011 and 3.0 km in 2008 in the first test, and 1.0 and 4.5 km in

the second. We held the survey geometry, regional field and analysis windows fixed (Online Resource 1, spatial_sensitivity).

With narrower strips, all 68 sign constraints held in 519 of 999 draws at the flown location and in 755 at one or more centers on the 1° grid. With wider strips, both counts were 740 of 999. At the flown location, only three 2011 target windows lost their negative slope. Lines 12350, 12360 and 12370 (7, 8 and 8 bins) retained it in 881, 690 and 705 draws with narrower strips and in 999, 740 and 740 with wider strips, respectively. All 14 northern windows and all 40 constraints from 2008 retained their signs in every draw at both scales. The five eastern raw slopes also retained their reversals after main-field subtraction in every draw. No control sector passed the grid test in any draw.

For Uruana, the 2.5th–97.5th percentiles of the best margin across the grid were −1.377 to +0.456 nT/km with narrower strips and −0.482 to +0.453 nT/km with wider strips. For the closest control, 14 km west, the corresponding ranges were −0.425 to −0.038 and −0.409 to −0.049 nT/km. Each 2008 band at Uruana spans five or six grid rows grouped into two or three strips. Instrument calibration also remained fixed in this test.

These fractions describe sensitivity conditional on the chosen residual perturbations, strip widths and fixed survey geometry. The 999 draws are not independent field replications or a null-model test of regional uniqueness. The five-line subtraction result and the full 68-constraint pattern are therefore reported separately.

5. Predicting historical profiles from the 2008 survey

5.1 Equivalent sources fitted to 2008

We divided the area covered by the Serra da Ilha and Buritis map sheets into 12 × 12 km tiles on a fixed grid centered on Uruana. For each tile we took 2008 grid nodes within 24 km of its center and subtracted the IGRF-14 intensity at each node. We evaluated the local main-field direction at each tile center. A horizontal array of 169 equivalent dipoles, spaced 4 km apart, lay 6 km below the nominal 2008 flight plane. We estimated signed coefficients for the dipoles while keeping their depth fixed.

At each grid node we predicted the scalar anomaly by projecting the summed dipole vectors onto the unit main-field direction. In the 2008 fit the dipole moments point along that same direction. We centered the response and the columns of the forward matrix, then estimated the amplitudes by ridge regression. We set the damping parameter to 0.03 times the largest singular value of the centered matrix. We used the same source positions, amplitudes and damping in both historical predictions.

$$\hat{c} = arg\,min_c \left(\|\tilde{A}c - \tilde{d}\|^2 + \lambda^2\|c\|^2\right), \quad \lambda = \alpha\sigma_{max}(\tilde{A}) \quad (2)$$

In Eq. (2), Ã and d̃ are the column-centered forward matrix and demeaned 2008 residuals, c contains the signed equivalent-source amplitudes, and σmax is the largest singular value. The primary fit uses α = 0.03. The source coefficients constitute a regularized representation of the scalar data; their signs and assumed directions do not establish a unique subsurface magnetization.

Both predictions used the historical coordinates and elevations. The fixed-field calculation retained the 2008 projection and moment directions and their 2008 strength. The epoch-specific calculation used the IGRF-14 direction at 1971.5 and the historical flight height for both projection and

induction. It multiplied the moments by the ratio of the historical field intensity to that at the 2008 flight plane. At the Uruana center the two modeled directions differ by 12.54° for historical elevation 0.79 km. The 2008 data alone determined the fitted coefficients.

5.2 Segment definition and score

We grouped historical readings by tile, production line, sheet and elevation. Eligibility required at least five points, 4 km east–west span and at least 60% of the nominal grid nodes within the training disk. At least 80% of the historical points had to be within 3 km of a 2008 grid node. The primary set retained segments for which every point lay at least 1 km from any historical point scored earlier in the Uruana–SAA analyses. We recorded these rules before scoring the additional segments, with the acquisition date and original central-footprint results already known.

Within each segment we subtracted the mean observed-minus-predicted residual, squared the remaining residuals and pooled them over individual points. The square root of their pooled mean gives the root-mean-square error (RMSE) in profile shape. Both predictions use the same points. Centering removes the effect of a constant offset on each segment. We also aggregated squared errors in fixed 24 × 24 km blocks. We recomputed the pooled improvement after dropping each block in turn to quantify the influence of individual blocks. The scripts, inputs and order of analytical decisions are documented in Online Resource 1.

6. Historical profile reconstruction

Using the archived coordinates, the historical field update reduced pooled profile-shape error from 2.6571 to 1.7966 nT across 608 points on 75 segments from 33 line identifiers. Sixty-nine segments lay on the Buritis sheet and six on Serra da Ilha. Section 6.2 repeats the comparison after datum correction. Fifty-six segments improved and nineteen worsened (Fig. 6a). Aggregating squared errors by geographic block favored the historical field in seven of nine blocks. Removing a single block at a time yielded reductions from 25.4% to 36.4%, compared with 32.4% for all nine together.

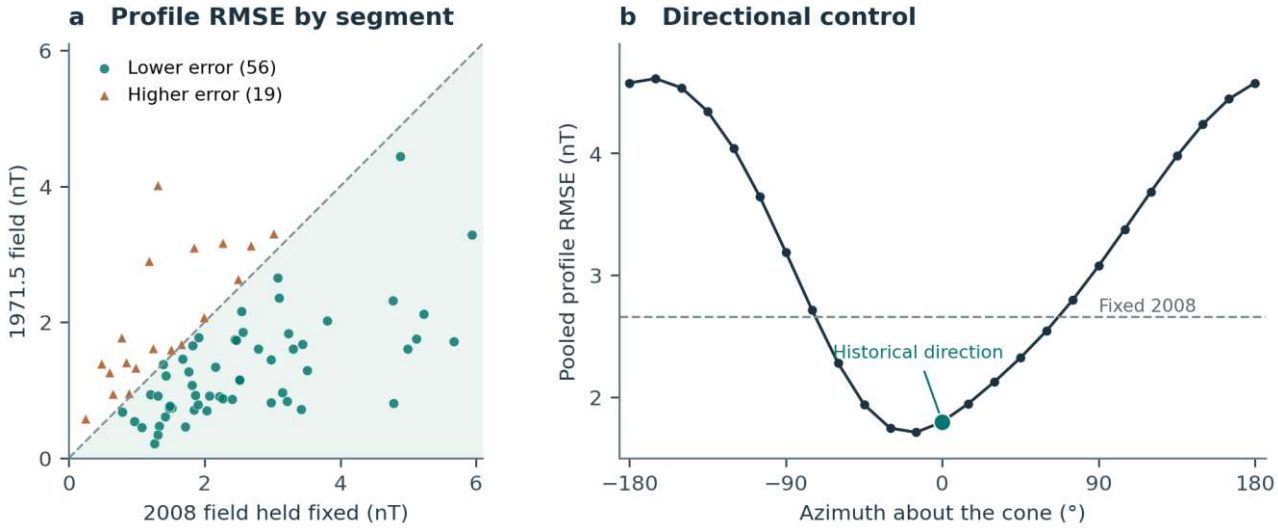


Fig. 6 (a) Paired errors on each primary segment. Points below the diagonal favor the historical field. Symbols distinguish the sign of the improvement. (b) Pooled error across 24 field directions with equal angular displacement from the 2008 field. Zero azimuth is the modeled historical direction. The two endpoints display the same direction. Code in Online Resource 1 (figures/fig.py)

6.1 Sensitivity to direction and survey trend

We rotated the historical direction about the 2008 vector in 15° steps around a cone while preserving both the three-dimensional angular separation and the historical field strength. The historical direction ranked third of 24 by error (Fig. 6b). The best cone azimuth was −15° (1.711 nT), while the opposite cone azimuth gave 4.578 nT. The lowest errors clustered around the historical direction.

A second diagnostic fitted a uniform east–west residual ramp separately for each field model, withholding the test block, its line identities and nearby training segments. After subtracting the calibrated ramp, the fixed and epoch-specific errors were 2.6502 and 1.6727 nT. The historical field retained its advantage after this trend correction. Across all 153 eligible segments (1,276 points, 49 lines), the uncalibrated errors were 2.8499 and 1.7667 nT. This set includes the primary evaluation segments and those scored in earlier work.

6.2 Geographic transfer within Brazil

We applied the fixed 2008 model to the wider overlap with project 1009. The source report identifies the historical coordinates as SAD69, the PGW magnetic channel as an IGRF-reduced residual and the WMC product as carrying an unknown arbitrary addition (Monteiro 2002). We used PGW and converted its coordinates to SIRGAS2000 with the IBGE transformation grid before projection to UTM 23S. The median shift on the local 75 segments was 67 m. Keeping their membership and source fits fixed gave 2.659 and 1.806 nT for the fixed and historical fields (32.1% reduction, 57/75 segments), versus 32.4% on the archived coordinates.

For the distant test we required every point to be at least 100 km from Uruana and 1 km from any previously scored point. Each new 24 km training disk had to stay at least 48 km center-to-center from all earlier fits. We split historical production runs by tile and elevation, at discontinuities in the stored row sequence and at position gaps above 4 km. All other coverage and source-fit rules were retained. The 1,528 eligible segments contained 16,746 historical observations on 539 previously unused line identifiers. Points lay 122–382 km from Uruana and at least 33 km from any previously scored point (Supplementary Fig. S1). All 267 new tile centers lay inside the 28 μT surface contour at both epochs.

Table 2 Pooled within-segment RMSE (nT) after datum correction. Projection only changes the observing direction, keeping the 2008 moments fixed. The full update also rotates and rescales the induced moments

Sample	Fixed 2008	Projection only	Full update
Nearby, 75 segments	2.659	1.951	1.806
Distant, 1,528 segments	15.429	14.701	14.871

After datum correction (Table 2), the full update improved 1,009 of 1,528 segments and 55 of 74 geographic blocks. Dropping one 24 km block at a time gave reductions of 2.7–5.7%. Resampling 25 whole 48 km blocks 20,000 times gave a descriptive 2.5th–97.5th percentile range of −0.2% to +8.4%. Shifting the block origin 24 km gave +0.7% to +8.0%. A flat-profile reference gave 20.822 nT. Projection alone gave the lowest pooled distant error. The full update outperformed projection alone in 40 of 74 individual blocks.

After applying a uniform east–west slope estimated separately for each model on the 75 nearby segments, distant RMSE fell from 15.482 to 14.909 nT (3.7%). Projecting out the individual linear slope of every distant segment gave 11.815 versus 11.390 nT (3.6%). This last comparison scores

curvature only. At the common barometric level of 0.95 km, the full update reduced error by 31.6% nearby and 11.6% farther away. Both samples lie within the same weak-field region and use the same acquisitions. They differ in baseline error and survey coverage. Holding segment membership, survey heights and the 2008 fits fixed, we also scored historical epochs 1971.0, 1971.5, 1972.0 and 1972.99. The reduction ranged from 32.04% to 32.19% nearby and from 3.52% to 3.89% farther away.

In an additional post hoc sensitivity analysis, we refitted the 2008 data at depths of 4, 6 and 9 km below the flight plane and relative damping levels of 0.01, 0.03 and 0.10, using the same grid as the orbital test in Section 8.2. The historical field and 75 datum-corrected evaluation segments were held fixed. The full epoch update reduced pooled error in all nine combinations, by 10.6–35.2%, with 49–59 of 75 segments improving. The primary 6 km, 0.03 configuration reproduced 32.1%. Across configurations, pooled RMSE ranged from 1.80 to 3.63 nT for the frozen field and from 1.38 to 3.18 nT for the full update; each gain compares predictions within the same configuration. Projection alone outperformed the full update in five of the nine settings. Thus the benefit of changing epoch is stable over this grid, while its magnitude and the additional benefit assigned to induced-moment rotation depend on the equivalent-source parameterization (Online Resource 1, historical_sensitivity). No setting was selected using these historical errors.

6.3 Historical prediction outside the South Atlantic weak field

The South NPR survey of 1977 and the Howard Pass–Misheguk Mountain survey of 2008 overlap in Alaska's Brooks Range (Brown 2012; Connard et al. 1999). We used this survey pair, previously examined for curvature orientation, to predict the 1977 profiles from the 2008 residual grid. We retained the Brazilian source spacing, depth, damping, tile size and coverage rules. We sampled the grid at 1.6 km and scored 250 m bins along north–south production lines. The primary calculation used nominal terrain clearances. Across 41 eligible tiles, modeled surface intensity was 56.6–57.2 μT over the two epochs, well above the 28 μT contour.

Table 3 Historical profile-shape prediction. Rotation is the median across eligible tiles. Error is the pooled within-segment RMSE in nT. Positive gain denotes a reduction in error

Region (segments)	Rotation	Fixed → updated	Gain
Uruana (75)	12.61°	2.659 → 1.806	32.1%
Distant Brazil (1,528)	12.89°	15.429 → 14.871	3.6%
Alaska (50)	1.43°	10.288 → 10.343	−0.5%

In Alaska, updating the field raised pooled profile-shape error and improved 14 of the 50 segments (1,922 bins, 19 line identifiers). Resampling seven 48 km blocks gave a descriptive gain range of −1.57% to +0.22%. Error also increased with a reconstructed terrain-following surface (0.53%), unshifted historical coordinates (0.57%) and 1 km bins (0.21%). The two Alaskan predictions differed by 0.248 nT RMS. Relative to the fixed-model error of 10.288 nT, this difference bounds the change in RMSE at 2.41% (Table 3).

In Brazil, the field update changed predicted profiles by 2.07 nT RMS near Uruana and 6.80 nT farther away. The correction aligned more closely with the original prediction error near Uruana (pooled vector cosine 0.74 versus 0.30). In a post hoc check, only six distant segments, all in one tile, fell within the nearby range of rotation (12.53–12.67°). At the common 0.95 km flight level, no

distant segment fell within the local range at that level. Rotation and site characteristics therefore vary together in this comparison.

Across the 60 Alaskan survey pairings in the archived selection table, the modeled rotation at the overlap centroid ranged from 0.25° to 2.48°, below the 12.53–12.67° interval near Uruana. The 1976–2017 Coleen–Porcupine pairing gave 2.45° from survey metadata. Online Resource 1 also reproduces the separate 1945–1946 and 1965 comparison of curvature axes from the archived tables.

6.4 Offshore matches to the historical rotation

We screened the global surface IGRF-14 at 1971.5 and 2008.5 for field intensity of at least 28 µT at both dates and the 12.53–12.67° rotation spanned by the 23 nearby Brazilian tile centers. All 879 eligible centers of a 0.125° grid were in the equatorial Atlantic (Fig. 7a). The largest rotation on mapped land at 1:110 million scale was 11.41° among centers meeting the intensity criterion. The 0.25° and 0.5° grids also placed every match offshore.

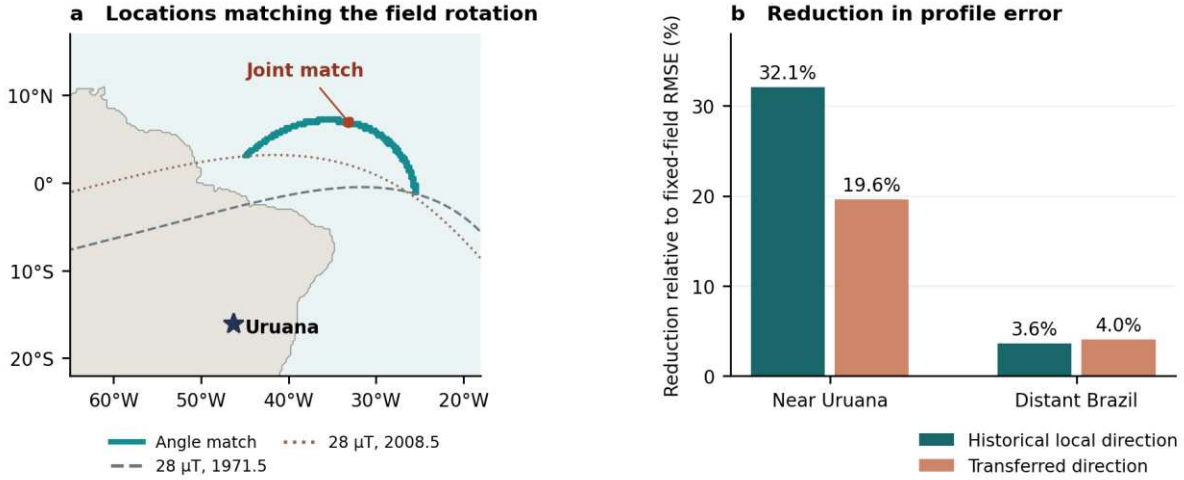


Fig. 7 (a) Teal marks locations matching the total rotation outside both 28 µT contours. The orange patch also matches the historical-to-modern intensity ratio. (b) The percentages use Brazilian profiles for both predictions. The comparison changes only the direction of the rotation. Code in Online Resource 1 (matched_rotation/figure.py)

Fifteen grid centers near 7°N, 33°W also matched the local historical-to-modern intensity ratio (1.0385–1.0401). From 1971 to 2008 their declination shifted east by 2.31–2.49°, whereas the 23 Brazilian centers shifted west by 4.23–4.36°. We expressed each offshore rotation from 2008 back to 1971 as a direction in the plane tangent to the 2008 field, using axes of increasing declination and inclination. At each Brazilian tile we substituted that direction while retaining the local starting vector, angle, historical strength and fitted sources. We selected the median offshore bearing before scoring the predictions.

Across 75 nearby segments, RMSE was 2.659 nT with the fixed field, 2.138 nT with the representative offshore direction and 1.806 nT with the historical local direction. All 15 alternatives gave 2.132–2.143 nT. Removing each segment's linear trend left 1.251 versus 1.001 nT. The local direction gave the lower curvature error in all nine blocks. Across 1,528 distant segments the offshore direction gave a lower pooled error than the historical local direction (14.810 versus 14.871 nT). Fig. 7b compares the percentage reductions in error relative to the fixed-field model in the two regions.

6.5 Directional resolution of the historical profiles

We repeated the directional test on datum-corrected coordinates using all 360 integer bearings in the tangent plane. A bearing of 0° points toward increasing inclination and +90° toward increasing declination during the update from 2008 back to 1971. Each segment retained its historical rotation angle and intensity ratio. We let the profile shape or its curvature select a single bearing across the region and compared the result with the historical field, which varies by tile and elevation.

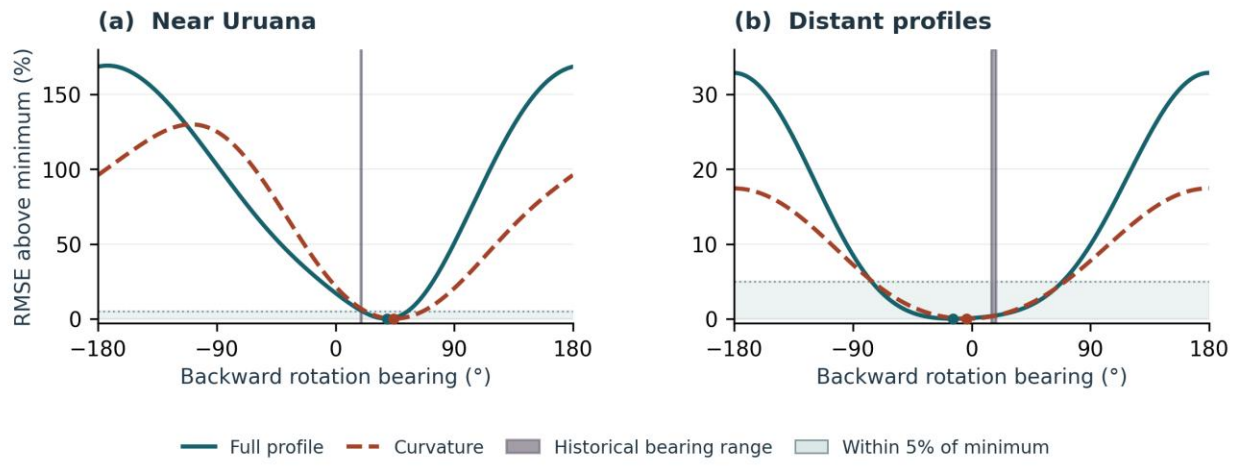


Fig. 8 Each curve gives its percentage increase in RMSE above its own minimum. The vertical scales differ. Dots mark the best grid bearing. The 5% band defines a descriptive tolerance for comparing the widths of the curves. Code in Online Resource 1 (directional_resolution/figure.py)

Nearby profile-shape error reached 1.713 nT at +39°. Bearings from +21° to +54° lay within 5% of that minimum (34 grid values). The historical bearing spanned +19.1° to +19.9° and gave 1.806 nT. On the local rotation cone the +39° solution lies 4.1–4.3° from the historical field vector. For distant profiles the minimum was at −14° and the same tolerance admitted 146 bearings (−76° to +69°). Curvature alone gave minima at +44° nearby and −4° farther away. At a common tolerance of 0.10 nT above the minimum, the full profiles admitted 37 nearby versus 68 distant bearings. For curvature, both admitted 63. Fig. 8 shows how quickly error rises on either side of each optimum.

For each held-out 24 km block we chose the bearing on other blocks, removing all shared line IDs and any calibration tile center within 24 km of a test center. Across nine nearby blocks, held-out RMSE was 1.775 nT against 1.806 nT with the historical field. Curvature errors were 0.957 and 1.001 nT. Requiring disjoint source-fit disks left seven testable blocks and preserved both pooled rankings. The distant shape optimum gave 2.179 nT when transferred to Uruana. Transferring +39° to distant profiles gave 15.013 nT against 14.871 nT with their historical field. The two regional fits shared neither flight-line IDs nor source-fit disks.

7. The 2008 model and the 2011 target gradient

Fig. 9a,b shows a historical profile that improved and one that worsened. We next used the central 2008 source fit to predict the gradient measured in 2011. We added the 2011 IGRF-14 background at each bin and altitude to the predicted source contribution. In the target cap, 6–8 km north of the center and within an 8 km radius, we computed the slope of intensity against grid north from 250 m bin medians on each of 14 target lines.

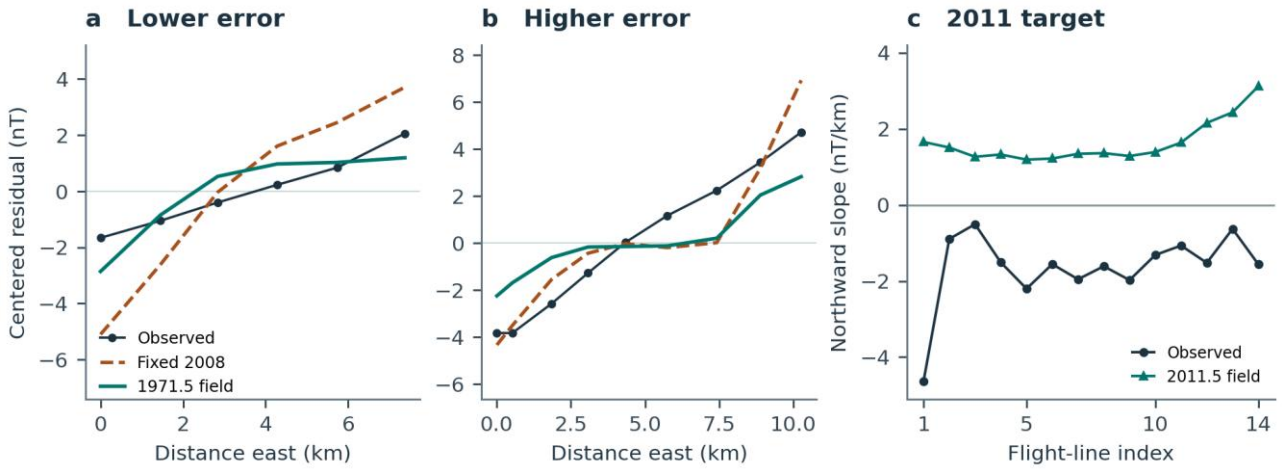


Fig. 9 (a,b) Example segments from 1971–1972 nearest to the median change in error within their respective improvement and worsening groups. They are Buritis lines 7.8 and 10.7, both at 0.95 km elevation. Each trace has its own mean removed. (c) The 14 target lines in 2011 ordered by line identifier. The central model predicts a positive northward slope on every line. All 14 measured slopes are negative. Code in Online Resource 1 (figures/fig.py)

Measured slopes ranged from −4.64 to −0.51 nT/km (median −1.54 nT/km). The epoch-specific predicted slopes ranged from +1.19 to +3.12 nT/km (median +1.38 nT/km). Keeping the measured local residual fixed and substituting the smooth 1971.5 background for the 2011 background preserved the negative sign on all 14 lines. The 2008 grid and downward continuation recovered part of the historical profile shape but predicted the wrong target sign on every 2011 line. Repeating the target prediction for both 2008 channels, source depths of 4, 6 and 9 km and relative damping of 0.01, 0.03 and 0.10 gave positive slopes on all 14 lines in all 18 configurations. This sensitivity grid did not resolve the discrepancy.

7.1 Recovery from off-grid sources

In a post hoc resolution audit, we used synthetic source locations distinct from the inverse-mesh nodes: one sphere, a pair of equal spheres and a seven-sphere chain, at nine center offsets and depths of 2, 4 and 8 km below the 2008 plane. The 81 geometries were evaluated with induced moments and two fixed remanent directions, giving 243 scenarios. The induced cases prescribe moments proportional to the main field; they do not model demagnetization or infer susceptibility. Synthetic observations used the 663 central 2008 grid nodes and the 110 measured target-bin positions and GPS heights in 2011. The source directions and strengths were specified independently of the inverse fit. The primary inverse depth and damping remained 6 km and 0.03. These tests evaluate transfer from the interpolated grid; they do not reproduce the original survey gridding or treat its nodes as independent flight observations.

We limited the anomalous vector field to 0.1% of the main field at every sampled position. This cap followed an explicit amendment after the initial training-RMS normalization produced strong-field cases; the original runs and decision record are retained. Exact vector addition changed no eligible truth-sign classifications and differed from the first-order target anomaly by less than 0.027 nT RMS in every amended scenario. Sign scores include only true total-field slopes with magnitude at least 0.1 nT/km. No synthetic target values select inverse parameters. Online Resource 1 reports all nine inverse configurations, two remanent directions, and white and 6 km-correlated noise at 5% and 20% of each scenario's training-signal RMS, with 20 realizations per condition. These amplitudes are experimental controls rather than measured survey uncertainties.

For the noiseless induced cases, the primary model recovered 254/367, 285/367 and 346/377 eligible signs at source depths of 2, 4 and 8 km: 69.2%, 77.7% and 91.8%, respectively (Fig. 10c). The median training RMSE divided by training-signal RMS was 61.7%, 18.7% and 2.8%. A background-only comparator gave 80.4%, 66.2% and 82.8% correct signs, outperforming the reconstruction for the shallowest sources. Of six induced scenarios with all 14 true slopes at or below −0.1 nT/km, only one recovered all 14 negative signs. At relative damping 0.03, increasing the inverse depth from 4 to 9 km reduces sign agreement for 2 km sources from 81.2% to 67.8%, while increasing it for 8 km sources from 33.2% to 92.8% (Online Resource 1, resolution_audit/synthetic_summary.csv). These controlled outcomes demonstrate resolution-dependent failures of local-gradient recovery even without measurement noise.

7.2 Conditional stability of the 2011 sign prediction

We next held the real 2008 data and each equivalent-source configuration fixed and minimized the same ridge objective J from Eq. (2), subject to predicted total-field slopes of at most −0.1 nT/km on all 14 target lines. This constructs the least-cost sign reversal inside the specified model family. The known sign pattern supplies the constraints, so the resulting model is a sensitivity example rather than a new prediction. For a coefficient perturbation δ about the unconstrained optimum ĉ, the excess objective is exactly quadratic:

$$J(\hat{c} + \delta) - J(\hat{c}) = \delta^T H \delta, \quad H = \tilde{A}^T \tilde{A} + \lambda^2 I \quad (3)$$

This identity permits analytic minimum and maximum slopes inside any specified objective envelope. We archived envelopes at 1.1, 1.5, 2 and 5 times the optimum objective, along with the simultaneous 14-line constrained solutions. The convex solutions satisfy the constraints and numerical optimality conditions; independently reconstructed matrices reproduce the primary objective identity. The envelopes are descriptive fit–regularization budgets, not confidence intervals derived from instrument noise. Signed equivalent-source coefficients and their norms do not establish geologically admissible magnetization.

For the primary configuration, the constrained slopes span −2.054 to −0.100 nT/km, while the unconstrained slopes span +1.191 to +3.118 nT/km (Fig. 10a). Training RMSE increases from 1.007 to 1.116 nT and the regularized objective by 8.4%. The fitted 2008 values change by 0.471 nT RMS. The coefficient-vector norm increases by 1.7%, but the perturbation itself is 19.6% of the original vector norm; these are different measures. Across the nine depth–damping configurations, all 14 signs can be reversed at objective increases of 0.5–16.8% (Fig. 10b), with fitting-RMSE increases of 0.045–0.186 nT.

The constrained solutions demonstrate that agreement among the tested unconstrained optima does not establish sign stability within this source family. The objective increase quantifies the cost of reversing the prediction. Determining which objective budget is observationally acceptable requires a calibrated survey-error model.

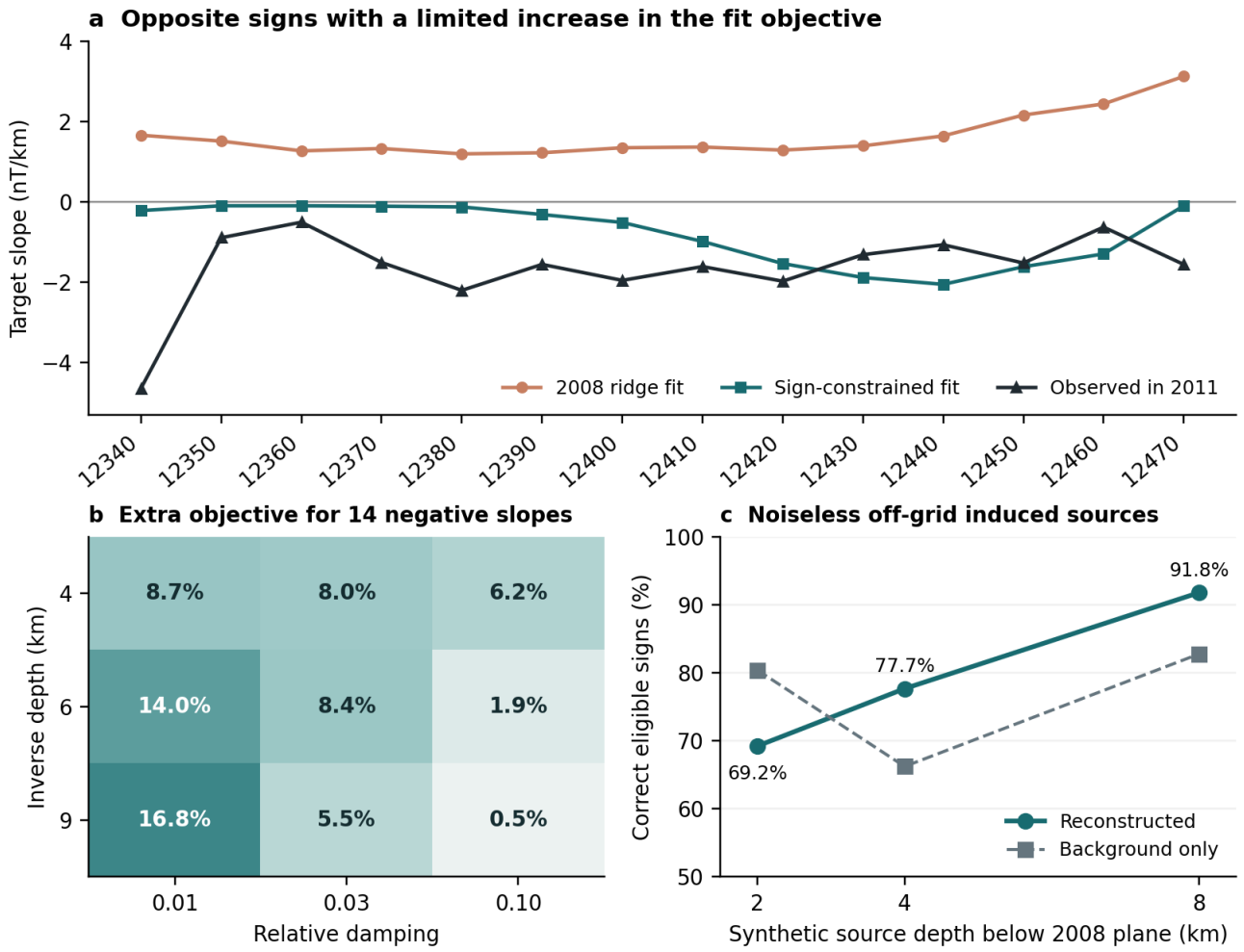


Fig. 10 Conditional stability and synthetic recovery of the target gradients. (a) Observations, the primary 2008 ridge prediction and the least-objective model constrained to slopes ≤ −0.1 nT/km on all 14 lines. The constrained curve is not an independent prediction. (b) Relative increase in the ridge objective needed to satisfy those constraints for each inverse depth and damping. (c) Sign agreement for 27 noiseless off-grid induced-source scenarios at each true depth; only truth slopes with magnitude ≥ 0.1 nT/km are scored. The dashed comparator uses the regional background alone. Code and every case are in Online Resource 1 (resolution_audit).

7.3 Predicting the gain from surface geology

Using the Serra da Ilha and Buritis maps (CPRM and COMIG 2002; Kuchenbecker et al. 2015), we tested whether alignment of mapped bedding with the previously identified 146° axis, or proximity to a mapped contact, predicted the segment-level gain above position, sheet, radius, height and grid coverage. We evaluated the models in withheld 24 km blocks and excluded common flight-line identifiers and training centers within 6 km of a test center. Bedding required two mapped localities within 8 km. Contacts were tested on the Buritis GIS. On Serra da Ilha only 98 of 148 map labels matched the unit colors extracted from the map, below the 85% threshold set for use. Results for faults also depended on the spatial trend (Table 4).

Table 4 Error in predicting the segment-level improvement in profile RMSE, in nT. The geographic baseline and the model with the map attribute are compared on the same segments. Lower values indicate better prediction of the gain

Map attribute and geographic trend	Segments	Baseline	With attribute
Bedding alignment, linear	65	1.2704	1.3032
Buritis contact proximity, linear	41	1.1524	1.1529
Buritis fault proximity, linear	41	1.1524	1.0063
Buritis fault proximity, quadratic	41	1.1598	1.3404

8. Interpretation and implications

8.1 The regional gradient and the local magnetic signature

Across the target, the local residual outweighs a positive regional gradient on every 2011 line. Farther north, subtracting the modeled long-wavelength core field reverses the positive slope on five adjacent eastern lines across all ten fits. Correcting for the lithospheric contribution resolved by EMM2017 leaves those slopes positive. In the raw least-squares fit, IGRF-14 subtraction reverses a sixth line. In 2008 the regional contribution restores the positive first band in both channels at all five corridor widths. The controlling quantity is the northward gradient. The 28 μT contour classifies intensity, and the modeled matches at Mocuba and other exterior longitudes show that the sign pattern extends beyond it.

The sector 14 km west matches the 2011 pattern at more locations than Uruana, yet none of its 2011 matches coincide with its 2008 matches. Among the 23 measured sectors, only Uruana matches both surveys on the tested grids. On the 1° grid, 731 locations preserve every sign across all ten fits. In the narrow-strip test, the complete pattern held at Uruana in 519 of 999 draws and at one or more grid centers in 755. Every loss at the flown location arose in one or more of three short target windows. The five eastern reversals persisted at both strip widths.

Near Uruana, the historical field direction predicts profile shape better than all 15 matched offshore directions. Fitting the bearing to nearby profiles reduces held-out error from 1.806 to 1.775 nT. At 122–382 km, changing projection alone gives the lowest pooled error (14.701 nT), followed by the full update (14.871 nT) and the fixed field (15.429 nT). The 48 km block resampling range for the gain from the full update spans −0.2% to +8.4%. For Brazilian survey compilations, the improvement from using the historical field is largest in the nearby profiles. All 60 Alaskan survey pairs span smaller field rotations than the Brazilian pair, so the comparison cannot separate rotation from location inside or outside the SAA.

The 2008 source model predicts a positive target slope on all 14 lines where the 2011 survey measures a negative slope. The resolution audit shows why stability across a small grid of inverse depths and damping values does not by itself certify sign stability: all unconstrained optima agree, but constrained solutions reverse every sign with a 0.5–16.8% increase in their respective objectives. The independent synthetic geometries also exhibit sign-recovery failures, including induced cases without noise. Together, these tests identify local-gradient recovery as a separate requirement for evaluating the reconstruction. Adding mapped bedding or proximity to contacts did not improve predictions of the historical error reduction, and the fault result changed sign with the spatial trend. Source interpretation still requires independent constraints on geometry and magnetization.

8.2 The modeled Uruana contribution at orbital altitude

To compare the scales of the local airborne signal and the regional anomaly, we continued the compact sources fitted to the central 2008 grid to 450 km altitude. Across 18 models spanning two channels, three equivalent depths (4, 6 and 9 km) and three relative damping levels (0.01, 0.03 and 0.10), the predicted vector magnitude was 0.00014–0.00144 nT. At the same location, height and epoch, full IGRF-14 intensity differs from centered-dipole intensity by about 5,396 nT. The largest orbital signal predicted from the local sources is less than one millionth of this regional intensity difference.

9. Conclusions

On five adjacent eastern lines at Uruana, subtracting the core field modeled by EMM2017 reverses the northern slope, while subtracting its resolved lithospheric contribution leaves every slope positive across five processing stages and two estimators. These five reversals survive all tested spatial perturbations. Among 23 measured sectors, only Uruana reproduces both survey sign sequences under common backgrounds; the complete pattern is less stable than the five-line result. Updating the field epoch reduces historical profile-shape error by 32.1% nearby and 3.6% farther away, with positive nearby gains across nine depth–damping settings. This historical benefit coexists with incorrect target signs in all 18 unconstrained 2011 predictions. Off-grid experiments expose resolution-dependent sign errors, and a constrained primary fit reverses all 14 signs while increasing training RMSE from 1.007 to 1.116 nT and the ridge objective by 8.4%. Thus, background attribution, historical prediction gain and local-gradient stability are separate outcomes. Evaluating them jointly establishes the scope of the reconstruction: the historical benefit is reproduced across the tested settings, while the local target signs remain sensitive to the source fit.

Statements and Declarations

Data and code availability

Online Resource 1 contains the analysis-ready data, field-model outputs, code, execution instructions, software versions and SHA-256 checksums for the reported analyses and figures. The Brazilian survey records are SGB/CPRM projects 1009 and 3087 and ANP project 0032. Connard et al. (1999) and Brown (2012) identify the Alaskan records.

SGB airborne catalogue · ANP onshore data · IGRF coefficients

Author contributions

Lucas Giovani Ribeiro contributed to conceptualization, methodology, software, formal analysis, data curation, visualization and writing the original draft. Marcos André Simonssini contributed to methodology, validation, and review and editing of the manuscript.

Funding

The authors received no external funding for this research.

Competing interests

The authors declare no competing interests.

Use of artificial intelligence

We used ChatGPT for writing and coding assistance, reviewed its output and take full responsibility for this work.

Supplementary information

Online Resource 1 Data, code and numerical outputs for regional-field decomposition, historical profile prediction and resolution tests at Uruana de Minas, including scripts for Figs. 1–10, Supplementary Figs. S1 and S2, reproduction instructions and file checksums

Figures were generated with Python and Matplotlib. Online Resource 1 provides the plotting scripts, software versions and inputs.

References

Beggan CD, Kloss C, Amblard P et al (2026) International geomagnetic reference field: the fourteenth generation. Earth, Planets and Space 78:127. https://doi.org/10.1186/s40623-025-02360-0

Brown PJ (2012) Aeromagnetic survey of Howard Pass quadrangle and the east half of Misheguk Mountain quadrangle, Alaska. U.S. Geological Survey Open-File Report 2009–1256. https://doi.org/10.3133/ofr20091256

Connard GG, Saltus RW, Hill PL, Carlson L, Milicevic B (1999) Alaska digital aeromagnetic database description. U.S. Geological Survey Open-File Report 99–503. https://doi.org/10.3133/ofr99503

CPRM and COMIG (2002) Folha Serra da Ilha, SE.23-V-B-I. Projeto São Francisco, geological map at 1:100,000. https://rigeo.sgb.gov.br/handle/doc/2354

Finlay CC, Kloss C, Olsen N et al (2020) The CHAOS-7 geomagnetic field model and observed changes in the South Atlantic Anomaly. Earth, Planets and Space 72:156. https://doi.org/10.1186/s40623-020-01252-9

Foroughi I, Goli M, Ferguson S, Pagiatakis S (2025) Geoid determination using airborne vector gravimetry: Insights from a real dataset. Studia Geophysica et Geodaetica 69:101–117. https://doi.org/10.1007/s11200-024-0748-5

Hartmann GA, Pacca IG (2009) Time evolution of the South Atlantic Magnetic Anomaly. Anais da Academia Brasileira de Ciências 81:243–255. https://doi.org/10.1590/S0001-37652009000200010

Kuchenbecker M, Costa RD, Gomes DGC, Gouveia GV, Figueiredo RA, Pimenta JS (2015) Folha Buritis, SD.23-Y-D-IV. Projeto Fronteiras de Minas Gerais, CODEMIG and UFMG. Geological map at 1:100,000 and GIS

Lesur V, Gubbins D (2000) Using geomagnetic secular variation to separate remanent and induced sources of the crustal magnetic field. Geophysical Journal International 142:889–897. https://doi.org/10.1046/j.1365-246x.2000.00190.x

Microsurvey Aerogeofísica e Consultoria Científica Ltda. (2011) Levantamento aerogeofísico de Minas Gerais, Programa 2010/2011, Área 19 Formoso–Buritis–Lagoa Grande. Relatório final do levantamento e processamento dos dados magnetométricos e gamaespectrométricos, vol I. CODEMIG and CPRM. https://geosgb.sgb.gov.br/downloads/index.php?dir=3087-Area19-Formoso_Buritis_Lagoa

Monteiro AC (2002) Convênio Geofísico Brasil–Alemanha, projeto 1009. Relatório das áreas digitalizadas pela PGW e WMC, pp 1–2. CPRM, Divisão de Geofísica, Rio de Janeiro. Distributed as Leia-me.pdf in the project 1009 XYZ archive

NOAA NCEI (2017) Enhanced Magnetic Model 2017 (EMM2017), spherical harmonic model. NOAA National Centers for Environmental Information. https://www.ncei.noaa.gov/products/enhanced-magnetic-model

Pavón-Carrasco FJ, De Santis A (2016) The South Atlantic Anomaly: The Key for a Possible Geomagnetic Reversal. Frontiers in Earth Science 4:40. https://doi.org/10.3389/feart.2016.00040

Poletti W (2021) The Earth's magnetic field of the last centuries from the perspective of the Jequitinhonha and Mucuri river valleys: A natural observatory of the South Atlantic Anomaly in Brazil. Journal of South American Earth Sciences 108:102984. https://doi.org/10.1016/j.jsames.2020.102984

Ribeiro LG, Simonssini MA (2026) The Uruana de Minas Geomagnetic Gradient Anomaly: A Structurally Locked Reversal Envelope Persistent Across Four Decades. Preprints.org, version 1 [preprint]. https://doi.org/10.20944/preprints202609.1201.v1

Vujić E, Brkić M (2016) Estimation of effect of unequal secular variation on geomagnetic data reduction. Studia Geophysica et Geodaetica 60:162–176. https://doi.org/10.1007/s11200-015-0823-z

Zuo B, Hu X, Leão-Santos M, Wang L, Cai Y (2020) Downward Continuation and Transformation of Total-Field Magnetic Anomalies Into Magnetic Gradient Tensors Between Arbitrary Surfaces Using Multilayer Equivalent Sources. Geophysical Research Letters 47:e2020GL088678. https://doi.org/10.1029/2020GL088678

Supplementary Files

This is a list of supplementary files associated with this preprint. Click to download.

- ESM1.zip